Published in final edited form as:
Inorg Chem. 2008 May 19; 47(10): 3969–3977. doi:10.1021/ic701251j.

Characterization of the Fe Site in Iron-Sulfur-Cluster-Free Hydrogenase (Hmd) and of a Model Compound *via* Nuclear Resonance Vibrational Spectroscopy (NRVS)

Yisong Guo[†], **Hongxin Wang**[‡,†], **Yuming Xiao**[†], **Sonja vogt**[¶], **Rudolf K. Thauer**[¶], **Seigo Shima**[¶], **Phillip I. Volkers**[⊥], **Thomas B. Rauchfuss**[⊥], **Vladimir Pelmentschikov**[£], **David A. Case**[£], **Ercan E. Alp**[§], **Wolfgang Sturhahn**[§], **Yoshitaka Yada**[¥], and **Stephen P. Cramer**[†,‡]

Yisong Guo: ; Hongxin Wang: ; Yuming Xiao: ; Sonja vogt: ; Rudolf K. Thauer: thauer@mpi-marburg.mpg.de; Seigo Shima: ; Phillip I. Volkers: ; Thomas B. Rauchfuss: rauchfuz@uiuc.edu; Vladimir Pelmentschikov: ; David A. Case: case@scripps.edu; Ercan E. Alp: ; Wolfgang Sturhahn: ; Yoshitaka Yada: ; Stephen P. Cramer: spcramer@lbl.gov

[†]Department of Applied Science, University of California, Davis, CA 95616

[‡]Physical Biosciences Division, Lawrence Berkeley National Laboratory, Berkeley, CA 94720

[¶]Max Planck Institute for Terrestrial Microbiology, Karl-Von-Frisch-Strasse, D-35043 Marburg, Germany

[⊥]Department of Chemistry, University of Illinois, Urbana, IL 61801

[£]Department of Molecular Biology, The Scripps Research Institute, La Jolla, CA 92037, USA

[§]Advanced Photon Source, Argonne National Laboratory, Argonne, IL 60439

[¥]JASRI, SPring-8, 1-1-1 Kouto, Mikazuki-cho, Sayo-gun, Hyogo 679-5198, Japan

Abstract

We have used ^{57}Fe nuclear resonance vibrational spectroscopy (NRVS) to study the iron site in the iron-sulfur-cluster-free hydrogenase Hmd from the methanogenic archaeon *Methanothermobacter marburgensis*. The spectra have been interpreted by comparison with a *cis*-$(CO)_2$-ligated Fe model compound, $Fe(S_2C_2H_4)(CO)_2(PMe_3)_2$, as well as by normal mode simulations of plausible active site structures. For this model complex, normal mode analyses both from an optimized Urey-Bradley force field and from complementary density functional theory (DFT) calculations produced consistent results.

Previous IR spectroscopic studies found strong CO stretching modes at 1944 and 2011 cm^{-1}, interpreted as evidence for *cis*-$Fe(CO)_2$ ligation. The NRVS data provide further insight into the dynamics of the Fe site, revealing Fe-CO stretch and Fe-CO bend modes at 494, 562, 590, and 648 cm^{-1}, consistent with the proposed *cis*-$Fe(CO)_2$ ligation. The NRVS also reveals a band assigned to Fe-S stretching motion at ~311 cm^{-1}, and another reproducible feature at ~380 cm^{-1}. The ^{57}Fe partial vibrational densities of states (PVDOS) for Hmd can be reasonably well simulated by a normal mode analysis based on a Urey-Bradley force field for a 5-coordinate *cis*-$(CO)_2$-ligated Fe site with additional cysteine, water, and pyridone cofactor ligands. A final interpretation of the Hmd NRVS data, including DFT analysis, awaits a 3-dimensional structure for the active site.

Correspondence to: Rudolf K. Thauer, thauer@mpi-marburg.mpg.de; Thomas B. Rauchfuss, rauchfuz@uiuc.edu; David A. Case, case@scripps.edu; Stephen P. Cramer, spcramer@lbl.gov.

Keywords

hydrogenase; *Hmd*; ^{57}Fe; nuclear resonant vibrational spectroscopy; NRVS; Mössbauer; synchrotron radiation; resonance Raman; normal mode; density functional theory; DFT

Introduction

The iron-sulfur cluster-free hydrogenase (Hmd) is only found in certain methanogenic archaea, and it catalyzes the reversible reduction of methenyltetrahydromethanopterin (methenyl-H_4MPT$^+$) with H_2 to methylenetetrahydromethanopterin (methylene- H_4MPT) and a proton [1–5]. In this reaction, a hydride is transferred from H_2 into the *pro-R* position of the methylene carbon of methylene-H_4MPT [3,6] (Chart 1). Although it was previously thought to be metal-free [4], Hmd is now known to harbor a mononuclear iron containing cofactor of unknown structure that is essential for activity [7,8].

The molecular ligation and electronic structure of the iron in Hmd remain elusive. Mössbauer experiments indicate that Hmd and its cofactor are diamagnetic in both the absence and presence of H_2 and/or methenyl-H_4MPT$^+$ [10], and this suggests low-spin Fe(0) or Fe(II) as possible electronic states. Infrared spectroscopy has provided evidence that in the as-isolated form the Fe in Hmd is bound to two CO molecules at approximately 90° to each other [11]. One additional CO or CN^- ligand can bind to the Fe [11], indicating a vacant or labile coordination site. Of the three conserved cysteine residues (Cys10, Cys176 and Cys250), only Cys176 is essential for enzyme activity [12]. Cys176 is also considered an attractive ligand candidate because it is positioned at an appropriate distance from the mononucleotide-binding site at the bottom of an intersubunit cleft [13]. Additional evidence for single cysteine coordination comes from the recent EXAFS analysis, which found 1 Fe-S interaction at 2.31 Å, along with 2 Fe-C at 1.80 Å and 1 N or O atom at 2.03 Å [12]. The latter might be provided by the Hmd organic cofactor.

Nuclear resonant vibrational spectroscopy (NRVS) is rapidly becoming a popular technique for probing the dynamics of Fe in metalloproteins [14,15]. This measurement involves scanning an extremely monochromatic x-ray beam through a nuclear resonance. Apart from the 'zero phonon' (recoil-free) Mössbauer resonance, there are transitions that correspond to nuclear excitation with creation (Stokes) or annihilation (anti-Stokes) of phonons. The NRVS intensity for a given normal mode is proportional to the motion of the resonant nucleus '*j*' (in this case ^{57}Fe) along the direction of the incident x-ray beam [15,16]. For a randomly oriented sample, a NRVS transition for normal mode α contributes a fraction ϕ to the normalized excitation probability $S(\bar{\nu})$ that is directly proportional to the Fe 'mode composition factor $e^2_{j\alpha}$ and inversely proportional to $\bar{\nu}_\alpha$ [16,17]:

$$\phi_\alpha = \frac{1}{3}\frac{\bar{\nu}_R}{\bar{\nu}_\alpha} e^2_{j\alpha}(\bar{n}_\alpha + 1) f \tag{1}$$

In the above equation, $\bar{\nu}_\alpha$ is the difference between the photon energy and the recoil-free nuclear resonance energy in wave numbers, $\bar{\nu}_R$ is the recoil energy $\bar{\nu}_R = \hbar^2 k^2/2m_{Fe}$ or ~16 cm^{-1}, $\bar{n}_\alpha = [\exp(hc\bar{\nu}_\alpha/k_B T)-1]^{-1}$ is the thermal occupation factor for a mode of frequency $\bar{\nu}_\alpha$ at temperature T [16], and the recoilless fraction f depends on $\langle x^2_{Fe} \rangle$, the mean square fluctuation of the Fe nucleus along the beam direction, *via* $f = \exp\left(-k^2 \langle x^2_{Fe} \rangle\right)$. It is also useful to define an ^{57}Fe-centered partial vibrational density of states (PVDOS), $D_{Fe}(\bar{\nu})$, using a lineshape function $\mathcal{L}(\bar{\nu} - \bar{\nu}_\alpha)$ [16,18]:

$$D_{Fe}(\bar{\nu}) = \sum_{\alpha} e^2_{Fe,\alpha} \mathscr{L}(\bar{\nu} - \bar{\nu}_{\alpha}) \quad (2)$$

The ^{57}Fe PVDOS can be extracted from the raw NRVS using the PHOENIX software package [19], and the Fe mode composition factor $e^2_{Fe,\alpha}$ for a given eigenvector α can be calculated from a normal mode analysis *via* the following equation, where m_i and $r_{i\alpha}{}^2$ are the mass of atom *i* and its mean square motion in mode α respectively [16,20]:

$$e^2_{Fe,\alpha} = \frac{m_{Fe} r^2_{Fe,\alpha}}{\sum_i m_i r^2_{i\alpha}} \quad (3)$$

In this paper we report the ^{57}Fe NRVS for the as-isolated form of Hmd from *Methanothermobacter marburgensis* (mHmd) under several different conditions. NRVS, far IR and resonance Raman spectra are also presented and analyzed for a mononuclear Fe complex with *cis*-$(CO)_2$ and thiolate ligation -$Fe(S_2C_2H_4)(CO)_2(PMe_3)_2$, normal mode calculations and DFT calculations were used to simulate the model complex NRVS spectrum. Normal mode calculations on a plausible model for the Hmd Fe site were used to reproduce and interpret the experimental data.

Experimental

Purification of ^{57}Fe-labeled Hmd

All of the Hmd samples were prepared from *Methanothermobacter marburgensis* grown in the presence of 50 μM $^{57}FeCl_2$ [10]. ^{57}Fe-enriched Fe metal (95.4%) was from Chemotrade (Düsseldorf). Hmd was purified from 100 g ^{57}Fe-grown cells (wet mass) *via* ammonium sulfate precipitation and Source 30Q anion-exchange chromatography followed by Sephadex G25 gel-filtration chromatography in H_2O for the removal of salts [11]. The resulting 13 mL Hmd solution had a protein concentration of approximately 10 mg/mL.

The activity of Hmd was measured at 40°C in 120 mM potassium phosphate buffer at pH 6.0 containing 1 mM EDTA and 20 μM methylenetetrahydromethanopterin (methylene-H_4MPT) [11]. The reaction was started by the addition of enzyme and followed photometrically *via* the increase in absorbance at 336 nm resulting from the formation of methenyl-H_4MPT^+ (ε_{336} nm = 21.6 mM^{-1} cm^{-1}). The ^{57}Fe-labeled Hmd had a specific activity of 600 U (μmol/min)/mg protein, which is the specific activity of fully active enzyme under the assay conditions. Tetrahydromethanopterin (H^4MPT) and methenyl-H^4MPT^+ were purified from *M. marburgensis* [21]. Methylene-H^4MPT was generated from H^4MPT and formaldehyde by spontaneous reaction.

Preparation of Hmd Samples for NRVS

In general, preparation of the samples was done in an anaerobic tent and under red light because of the oxygen and light sensitivity of Hmd. Samples were prepared at pH 8.0 under 5%H_2/95% N_2 (gas phase in the anaerobic tent) and at pH 6.0 + methenyl-H_4MPT^+ under 100% H_2. The equilibrium of the Hmd-catalysed reaction favors formation of methylene-H_4MPT from methenyl-H_4MPT^+ and H_2 at pH 8.0 and the reverse reaction at pH 6.0 ($\Delta G^{\circ\prime} = -5.5$ kJ/mol), which is why most spectroscopic analyses of Hmd have in the past been performed either at pH 8.0 or at pH 6.0. In this respect it is also important to know that Hmd from *M. marburgensis* is more soluble at pH 8.0 than at pH 6.0 and that methenyl-H_4MPT^+ is much

more stable at pH 6.0 than at pH 8.0. At pH 8.0 methenyl-H_4MPT^+ spontaneously hydrolyses slowly to N^{10}-formyl-H_4MPT.

pH 8.0 Hmd

Purified Hmd (10 mg/mL) was supplemented with Tricine-NaOH pH 8.0 (pH at 0°C) to a final buffer concentration of 50 mM and concentrated by ultra-filtration using Amicon-Ultra-15 membranes (10 kDa cutoff) to a protein concentration of 320 mg/mL (8 mM). Hundred μl aliquots of the concentrate were transferred into 7 mL vials closed with a rubber stopper and filled with 5%H_2/95%N_2. After incubation at room temperature for 20 min, 50 μl samples were transferred into Lucite NRVS cuvettes (3×7×1 mm^3 interior) and quickly frozen in a liquid nitrogen bath. The cuvettes with the samples were stored in a dewar filled with liquid nitrogen.

pH 8.0–$H_2{}^{18}O$ Hmd

Purified Hmd (10 mg/mL) was supplemented with Tricine-NaOH pH 8.0 to a final buffer concentration of 50 mM and concentrated using Amicon-Ultra-15 membranes to a concentration of 320 mg/mL. Hundred μl aliquots of the concentrated solution were completely dried *via* anoxic evaporation for 60 min in a vacuum system equipped with a cold trap. The enzyme was then redissolved in $H_2{}^{18}O$ in 7 mL vials closed with a rubber stopper and filled with 5%H_2/95%N_2. Activity measurements on the redissolved enzyme did not show a significant decrease in Hmd activity. After two hours on ice, duplicate 50 μl samples were transferred into NRVS cuvettes, quickly frozen in a liquid nitrogen bath, and stored in a dewar filled with liquid nitrogen.

pH 6.0 Hmd + methenyl-H_4MPT^+ + H_2

Purified Hmd (10 mg/mL) was supplemented with Mes-NaOH pH 6.0 (pH at 0°C) to a final concentration of 50 mM and concentrated using Amicon-Ultra-15 membranes to a concentration of 320 mg/mL. Eighty μl aliquots of the concentrate were transferred into 7 mL vials closed with a rubber stopper and filled with 100% H_2. Then, 20 μl 30 mM methenyl-H_4MPT^+ solution was added. After incubation at room temperature for 20 min, 50 μl samples were transferred into NRVS cuvettes, and these placed into a bottle which was then closed with a rubber stopper and filled with 100% H_2. After 12 hours at 4 °C the bottle with the NRVS cuvettes was placed into a deep freezer at −80 °C for 12 hours. Subsequently the frozen samples in NRVS cuvettes were quickly transferred into a liquid nitrogen bath, and then stored in a dewar filled with liquid nitrogen.

Mössbauer Spectroscopy

After the NRVS measurements were completed, the samples were examined by Mössbauer spectroscopy in an Oxford OptistatDN cryostat at 77K without a magnetic field. The spectrometer consisted of a Wissel 1200 Mössbauer velocity drive, a proportional counter detector, and a room temperature ^{57}Co/Rh source. The spectra were calibrated by reference to the spectrum of a room temperature 25 μm α-Fe foil. 84.2% of the pH 8.0 sample Mössbauer signal could be simulated with an isomer shift δ of 0.06 mm s^{-1} and a quadrupole doublet ΔE_Q of 0.66 mm s^{-1}. This corresponds to values reported for the pH 8.0 holoenzyme [10]. Approximately 12.8 % of the sample was simulated by δ=0.28 mm s^{-1} and ΔE_Q=1.36 mm $^{-1}$, and ~3% of the sample was simulated by δ=1.35 mm $^{-1}$ and ΔE_Q=2.97 mm s^{-1}. The doublet with δ=0.28 mm s^{-1} definitely is not Hmd with extrinsic bound CO, since the latter species has a δ=−0.03mm/s [10]. It may represent Hmd with one (or both) of the intrinsic CO ligands dislodged. This minor impurity may have formed during sample preparation, during the NRVS experiment, or in the course of shipping and handling. We tend to discount radiation damage, since the flux density in NRVS experiments is almost 4 orders of magnitude below that used for EXAFS measurements. Nevertheless, at the 13% level it does not alter our main

conclusions. The 3% component has parameters similar to those of nonspecifically bound high-spin ferrous ions found in light-inactivated Hmd [10].

Synthesis and Crystallography of $Fe(S_2C_2H_4)(CO)_2(PMe_3)_2$

An acetone-THF solution prepared from $FeCl_2$ and two equivalents of PMe_3 was found to absorb CO to give an orange-red CO complex. Addition of $Na_2S_2C_2H_4$ gave $Fe(S_2C_2H_4)(CO)_2(PMe_3)_2$, **1** (eq 4)

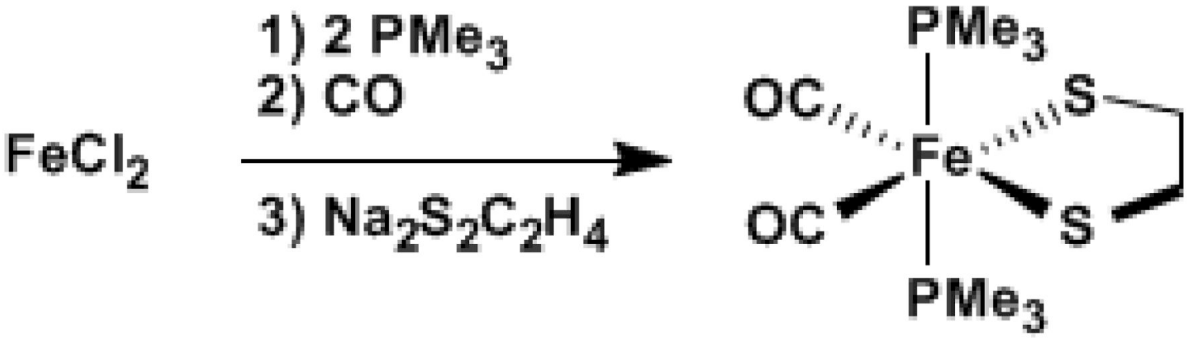

(4)

Under an atmosphere of CO, a 0 °C solution of 508 mg (4 mmol) of $FeCl_2$ in 70 mL of acetone was treated with a solution of 1 mL of PMe_3 (760 mg, 10 mmol) in 20 mL of THF. An initially formed yellow solid dissolved upon warming to room temperature and the reaction mixture became cloudy after *ca.* 15 min. After stirring for 30 min, IR analysis indicated the presence of a carbonyl-containing intermediate (acetone solution, *ν*CO, cm^{-1}): 2055 (w), 1987 (w), 1933 (s). The mixture was treated dropwise with $Na_2S_2C_2H_4$ which had been prepared from 565 mg (6 mmol) of $C_2H_4(SH)_2$ and 216 mg (9 mmol) of NaH in 5 mL of THF. After 50 h, the carbonyl-iron dithiolate mixture was filtered, and the orange-red filtrate was evaporated. The red residue was extracted into 8 mL of toluene, and the extract was layered with hexane. Storage overnight at −20 °C afforded red and orange crystals of diffraction quality. Yield: 867 mg (61%).

The ^{31}P NMR spectrum established equivalent PMe_3 ligands, consistent with the ^{1}H NMR spectrum that showed a triplet for the phosphine methyl group. Related complexes, of the type $Fe(CO)_2(PMe_3)_2RR'$ (R,R′ = CH_3, Ph, $CH{=}CH_2$) [22], contain *trans* phosphine ligands and display similar spectroscopic behavior. Thus, the phosphine ligands in **1** were mutually *trans*, suggesting *cis*-CO ligands, as supported by IR spectroscopy. The complex was further characterized by x-ray crystallography, which confirmed the stereochemistry indicated by the NMR and IR spectroscopies (Supplementary Material). Solid-state IR spectra of **1** are surprisingly complex in the *ν*CO region, presumably due to interactions between molecules within the unit cell. Thus, KBr pellets, and similarly Nujol mulls (see Experimental), of **1** exhibit bands at 1999, 1986 (sh), 1950, 1941, and 1934 cm^{-1}. Notice that these bands are clustered around the two, equally intense bands seen in toluene solution: 1998 and 1939 cm^{-1}. To rule out the occurrence of mechanochemical or tribochemical phenomena, unpulverized crystalline sample was analyzed by reflectance IR spectroscopy, and the sample again displayed the multiple-band spectrum. Dissolution of such samples in toluene gave the sharp two-band pattern. Toluene solutions of 1 are stable for hours at room temperature, although upon prolonged storage in solution the compound isomerized to the all-*cis* isomer as indicated by ^{1}H and ^{31}P NMR spectra.

^{1}H NMR (C_6D_6): δ 2.69 (s, 4H, SC_2H_4S), 1.20 (t, 18H, PMe_3, J = 4Hz). ^{31}P NMR (C_6D_6): δ 10.87. ESI-MS (m/z): 329 [M^+-CO, 20%], 301 [$(M\text{-}2CO)^+$, 100%]. IR (toluene, cm^{-1}): 1998 (vs), 1939 (vs). IR (Nujol, cm^{-1}): 1999 (s), 1984 (sh), 1950 (ms), 1933 (m), and 1910 (w). Anal. Calcd for $C_{10}H_{22}FeO_2P_2S_2$ (found): C, 33.72 (33.85); H, 6.23 (6.17).

Far Infrared Spectroscopy

IR spectra from 100-2000 cm^{-1} for $Fe(S_2C_2H_4)(CO)_2(PMe_3)_2$ were recorded at room temperature using a Brücker IFS 66 v/S FT-IR spectrometer. The sample chamber was maintained at 1 torr to minimize absorption by water vapor. The scanning speed was 10 KHz and the energy resolution was 4 cm^{-1}. The measurements were performed with different combinations of beamsplitters, detectors, sample preparation, and sample cell windows to optimize in each wavelength region. Far-IR spectra (100-500 cm^{-1}) were recorded with a 6 μm Mylar beamsplitter and a liquid He cooled Si bolometer. The sample was prepared as a Nujol mull in an anaerobic glove box, and sealed between polyethylene windows. The spectrum for the 400-700 cm^{-1} range was prepared in the form of KBr mixture sealed with polyethylene windows and measured with KBr beamsplitter and Si bolometer. The spectrum in the 600-2000 cm^{-1} range was measured using KBr beamsplitter, MCT detector, KBr as sample medium material, and ZnSe windows. Individual regions were then normalized to each other and combined into one spectrum.

Resonance Raman Spectroscopy

Spectra were recorded on neat powders obtained from crushed crystals in backscattering geometry with a SPEX 1877 triple spectrometer at 6 cm^{-1} resolution, using ~20 mW excitation at 514.5 nm by a Coherent Innova 70-2 Ar+/Kr+ laser and a LN_2 cooled Spectrum One 594 CCD detector. Spectra were calibrated by reference to a liquid CCl_4 spectrum using the bands at 218 and 314 cm^{-1}.

Nuclear Resonant Vibrational Spectroscopy

^{57}Fe NRVS spectra were recorded using published procedures [15] on multiple occasions at beamline 3-ID at the Advanced Photon Source (APS) [23] and beamline 9-XU at SPring-8, Japan [24]. The APS provided ~ 2.5×10^9 photons/sec in 1 meV bandwidth at 14.4125 keV in a 1 mm (vertical) × 3 mm (horizontal) spot. The APS monochromators consisted of a water-cooled diamond (1,1,1) double crystal monochromator with 1.1 eV bandpass, followed by separate Si(4,0,0) and Si(10,6,4) channel-cut crystals in a symmetric geometry. The flux at SPring-8 was ~ 3.2×10^9 in a 1.1 meV bandwidth; the monochromators there consisted of a liquid N_2-cooled Si(1,1,1) double crystal monochromator, and asymmetrically cut Si(5,1,1) and Si(9,7,5) crystals. During NRVS measurements, samples were maintained at low temperatures using liquid He cryostats. Temperatures for individual spectra were calculated using the ratio of anti-Stokes to Stokes intensity according to: $S(-E) = S(E)\exp(-E/kT)$. Spectra were recorded between −30 meV and 90 meV in 0.25 meV steps. Delayed nuclear fluorescence and Fe K fluorescence (from internal conversion) were recorded with a single avalanche 1 cm^2 square photodiode (APD) at the APS and with an APD array at SPring-8 [25]. Each scan required about 40 min, and all scans were added and normalized to the intensity of the incident beam.

Normal Mode Calculations

The normal mode calculations were carried using a modification of program ‘Vibratz’ [26, 27], using a Urey-Bradley force field.

DFT Calculations

Our density functional theory (DFT) calculations closely follow those we have used previously [28]. The two functionals PWPW91 [29] and B3LYP [30] were alternatively used, as implemented in the JAGUAR V6.5 software [31]. All the calculations were done using LACV3P**+ basis set of triple-ζ quality with implicit treatment of the Fe core electrons ($1s^2 2s^2 2p^6$) using effective core potential (ECP) [32] for Fe atom. A single set of polarization functions was added on all atoms except Fe atoms (** option); diffuse functions were added on all atoms except H (+ option). All geometry optimizations were done using JAGUAR V6.5. Optimized structures and wave functions were exported to GAUSSIAN 03 [33] software for vibrational frequency calculations, with the non-default NRVS-relevant ^{57}Fe isotope mass set for the iron center. Each mode is assigned an intensity given by the fraction of its kinetic energy coming from the Fe atom. Simulated spectra were then prepared by convolution with a Gaussian line shape function having a width of 6 cm^{-1} (chosen to mimic the experimental resolution).

Results

Model Compound Spectra

We first discuss the vibrational spectra for the model compound $Fe(S_2C_2H_4)(CO)_2(PMe_3)_2$. In this mononuclear complex, the low-spin Fe(II) center is coordinated by two mutually *trans* trimethylphosphines, two *cis* CO, and the sulfur atoms of the chelating ethanedithiolate ligand, and it thus serves as a spectroscopic model for Fe bound by thiolate and *cis* CO ligands. For this complex, strong PVDOS features occur at 624, 598, 556, and 502 cm^{-1} (Figure 1). The three highest frequency bands are matched by the three strongest bands in the far IR absorption spectrum and by relatively weak peaks in the resonance Raman spectrum. In contrast, the 502 cm^{-1} mode seems to have no IR intensity, and it is not a resolved feature in the Raman spectrum. Reference to the extensive body of work on Fe carbonyl bending and IR and Raman spectra [34–41] allows these features to be qualitatively assigned as Fe-C-O bending and stretching modes. The higher frequency pair is expected to involve primarily Fe-C-O bending, while the lower frequency pair primarily reflects Fe-CO stretching motion. An IR/Raman peak is also seen at 672 cm^{-1}, but the very low NRVS intensity indicates almost complete lack of Fe motion in this mode.

At lower frequencies, the strongest Raman band falls at 484 cm^{-1}. This feature is weak in the IR and barely observable as a shoulder in the NRVS. These factors are consistent with assignment as a symmetric P-Fe-P stretching mode mixing with PC_3 stretching. A peak at 363 cm^{-1} in the NRVS and far IR spectra is assigned to asymmetric Fe-P stretching, by comparison with similar assignments for $Fe(CO_2)(PMe_3)_4$ [42]. Likely Fe-S stretching features are seen between ~270–340 cm^{-1} in both NRVS and far IR spectra. The intensity between 100 and 200 cm^{-1} derives primarily from Fe-P-C, Fe-S-C, and S-Fe-S bending motions, whereas features below 100 cm^{-1} are torsional and acoustic modes.

Model Compound PVDOS Simulations

Although DFT calculations have recently been successful in predicting NRVS spectra [28, 43,44], the absence of an Hmd crystal structure makes a DFT analysis difficult. Instead, we chose to first refine an empirical force field based on our $Fe(S_2C_2H_4)(CO)_2(PMe_3)_2$ model compound, to investigate reasonable force constants for low-spin Fe(II) with two CO ligands. DFT calculations using PWPW91 and B3LYP functionals and the LACV3P**+ basis set were also done to compare with the empirical force field simulation. Both DFT calculations used their own geometry-optimized structures, but the structural differences with the crystal structure were minimal. Simulations using the empirical force field or DFT with B3LYP and PWPW91 functionals are presented in Figure 2. Key force field parameters, a summary of the

empirical normal mode analysis, and a comparison of diffraction *vs.* DFT bond lengths are included in Tables S1, S2, and S3, respectively. Major contributions to the normal modes are shown as PED curves in Figure S6.

In our empirical force field simulation, the two highest frequency NRVS bands of Fe$(S_2C_2H_4)(CO)_2(PMe_3)_2$ were found to have >80% Fe-C-O bend character. The peak at 624 cm^{-1} was found to result from overlap of two symmetric Fe-C-O bending modes – one at 626 cm^{-1} for motion in the 'equatorial' plane and one at 623 cm^{-1} for motion perpendicular to the 'equatorial' plane. In our force field, the small splitting of these modes is due to the steric interaction between the two CO ligands, which makes CO out-of-plane bending a little easier. The band at 598 cm^{-1} was simulated as mostly asymmetric Fe-C-O bending. In the DFT simulations, the highest frequency NRVS band (at 636 cm^{-1} using PWPW91 and at 630 cm^{-1} using B3LYP) was contributed mainly by Fe-C-O symmetric in-plane bending, while Fe-C-O symmetric out-of-plane bending contributed mainly at the second highest frequency band (at 607 cm^{-1} using PWPW91 and at 600 cm^{-1} using B3LYP), which gave a larger splitting of these two symmetric bending modes than the force field simulation.

The next two peaks at 502 and 556 cm^{-1} are simulated by modes that are primarily Fe-CO stretching in the Vibratz calculation. In the DFT calculations, these two peaks were predicted at 533 cm^{-1}, 583 cm^{-1} in PWPW91, and at 500 cm^{-1}, 552 cm^{-1} in B3LYP. At lower energies, as expected, the 363 cm^{-1} peak derives from Fe-P motion (mixed with P-C stretching), while the peak at 271 cm^{-1} derives mainly from Fe-S stretching motions mixed with P-C bending. These results were also consistent with DFT calculations, which simulated Fe-P asymmetric stretching at 350 cm^{-1} for PWPW91 and at 348 cm^{-1} for B3LYP, and Fe-S stretching mixed with Fe-P stretching, Fe-S-C, Fe-P-C bending at 254 cm^{-1} for PWPW91 and at 252 cm^{-1} for B3LYP. Other Fe-S stretching features are assigned between 250 and 350 cm^{-1}.

In the low frequency region, intensity between 100 and 180 cm^{-1} is primarily from Fe-P-C, S-Fe-S, and Fe-S-C bending motion, while C-Fe-C bending motion contributed at 103 cm^{-1}. On the high end, the simulations were able to model the IR active mode at 672 cm^{-1} as primarily due to P-C stretching motion, hence the lack of significant NRVS intensity. The CO force constants were also adjusted to match the CO stretching region, although they had little impact on the NRVS (Table S1).

Hmd NRVS Spectra

The ^{57}Fe PVDOS spectra for Hmd under several conditions are presented in Figure 3. We focus first on the features common to all of the spectra. In each case, the strongest band in the spectrum is at ~648 cm^{-1}. In the model complex, the highest frequency mode at 624 cm^{-1} was assigned to a symmetric $\delta Fe(CO)_2$ bend mode, and a similar assignment seems likely for Hmd. Similarly, all of the Hmd NRVS spectra have a strong feature at 494 cm^{-1} (with a low frequency shoulder), and by analogy with the model compound band at 502 cm^{-1}, this feature is attributed to a $\nu Fe(CO)_2$ stretching mode. The 494 and 648 cm^{-1} bands bracket additional features (520, ~562, 590 cm^{-1}) that appear in all of the spectra, albeit with variable relative intensities. Some of this variability may arise from the limited statistics of these preliminary data.

The region between 250 and 494 cm^{-1} is the likely range for Fe-S and Fe-O stretching modes. Here we found some common features as well as some significant changes. The strongest band in this region is at 311 cm^{-1}. This band is observed in all of the spectra and is tentatively assigned as an Fe-S stretching mode. Another peak at ~ 379 cm^{-1} is clearly seen in the pH 8 and pH 6 spectra, but it is somewhat weaker and broader in the $H_2{}^{18}O$ spectrum. Below 250 cm^{-1}, Hmd exhibits a relatively broad envelope of intensity, which does not return to baseline. The features down to 200 cm^{-1} would be consistent with Fe-pyridone stretches [39], while the intensity below 200 cm^{-1} presumably comes from bending and torsional modes of the Fe site.

By analogy with rubredoxin, below 100 cm^{-1} there will also be features involving motion of the Fe site with larger regions of protein [45].

Hmd Normal Mode Analysis

For a more quantitative interpretation of the Hmd PVDOS, we built several 4- and 5-coordinate models for the Fe site, based on distance and geometry constraints from recently published IR [11] and EXAFS [12] analyses respectively. Thus, all our models contained 2 CO ligands at 90° angles to each other, in accord with the mid-IR results [11], a cysteine (presumably from conserved Cys-176) with a 2.31Å Fe-S distance [12], and a pyridone ring with a 2.03Å Fe-N bond length (as a proxy for cofactor ligation). For simplicity we refer to the distorted tetrahedral structure in Figure 4 as our 'tetrahedral' model. Since Hmd is known to have a vacant or labile coordination site (because it can bind CN- or an additional CO ligand), we also built trigonal bipyramidal models both with and without a bound water molecule at the fifth coordination site (Figure 4). We refer to the truncated trigonal bipyramidal structure that lacks a water ligand as our 'truncated' model.

Starting with empirical Urey-Bradley force field parameters from the $Fe(S_2C_2H_4)(CO)_2(PMe_3)_2$ simulation as well as other work (Table S1), we calculated the expected PVDOS for these different models. The force field parameters were then adjusted to optimize agreement between the main peaks in the experimental and calculated $D_{Fe}(\bar{\nu})$ spectrum. Comparisons between experimental and calculated $D_{Fe}(\bar{\nu})$ are shown in Figure 4, the parameters employed are summarized in Table S1, and the potential energy distributions for representative normal modes of the 5-coordinate model are reported in Table S2. The potential energy distribution (PED) curves associated with these simulations are displayed in Figures S7, S8, and S9.

All of the simulations do reasonably well at reproducing the frequencies of the PVDOS peaks above 450 cm^{-1} (Figure 4), but the 'truncated' and trigonal bipyramidal models show better agreement with the peak intensities. The simulations also yield insight into the nature of the PVDOS features. In the trigonal bipyramidal simulation, the calculated peaks at 493 cm^{-1}, 558 cm^{-1}, 591 cm^{-1}, and 648 cm^{-1} correspond to modes that primarily involve Fe-CO stretching and Fe-C-O bending. Weaker features at 469 cm^{-1}, 515 cm^{-1}, 533 cm^{-1}, and 620 cm^{-1} are predicted to involve not only Fe-CO interactions, but also to have contributions from cysteine side chain and pyridone ring motion. Thus, although the CO ligands are perpendicular to each other in all the structures, the coupling of Fe-CO modes with other ligand modes changes with the Fe site geometry.

At lower frequencies, all of the simulations assign a large Fe-S stretching component to the features at ~274 cm^{-1} and ~311 cm^{-1}. We note that in the model compound simulations there are bands with Fe-S character between ~250–363 cm^{-1}, so assignment of the 274 and 311 cm^{-1} features appears settled.

The most problematic feature is a peak around 379 cm^{-1}, for which both Fe-Scys and Fe-OH2 stretching are plausible assignments. First of all, the 'tetrahedral' simulation shows almost no intensity in this region, and this seems to argue against such a geometry. In the trigonal bipyramidal simulation, the mode associated with this peak has 17% Fe-O stretching character in its PED. It also shifts by ~5cm^{-1} with ^{18}O substitution, which would be consistent with partial replacement in our experiment with ^{18}O water. However, the simulation for the 'truncated' model without a water ligand can also reproduce the 379 cm^{-1} feature, in which case the small differences with ^{18}O water would be dismissed as simply experimental noise. Without better statistics, it seems prudent to defer analysis of these small spectral differences, as well as weaker features in this region.

The last region of stretching modes, between ~200-250 cm^{-1}, is presumed to have a large Fe-N(pyridone) contribution in all three models. The spectra are quite broad in this region, preventing a detailed analysis. In the future, with better data this region might shed light on conformational changes in Fe-cofactor ligation.

Discussion and Conclusions

In this study we have applied the NRVS technique to two different $Fe(CO)_2$ moieties, the Fe site in Hmd hydrogenase and the $Fe(S_2C_2H_4)(CO)_2(PMe_3)_2$ model compound. The model compound study helped in several respects. It highlighted the special NRVS resulting from the presence of a *cis*-$Fe(CO)_2$ moiety, namely the presence of multiple strong bands between 500 & 650 cm^{-1}. The Urey-Bradley force field analysis of this complex also allowed us to establish reasonable parameters for FeCO stretching and bending force constants. In fact, the two different Fe-CO stretch constants used for Hmd, 3.64 and 2.60 mdyn $Å^{-1}$, almost symmetrically bracket the 3.15 mdyn $Å^{-1}$ value used for the model complex. The 1.14 mdyn $Å^{-1}$ Fe-S stretch constant for the Hmd simulation differed by <7% from the 1.22 mdyn Å–1 value used for the model compound.

Comparison of the DFT predictions for the $Fe(S_2C_2H_4)(CO)_2(PMe_3)_2$ NRVS *vs.* the experimental data allowed us to gauge the quality of agreement to be expected when a DFT calculation is using the correct structure. The DFT simulations using the two commonly accepted PWPW91 and B3LYP functionals produced NRVS spectra in good agreement with the experiment (Figure 2). Calculations using PWPW91 showed blue shifts of up to ~30 cm^{-1} for the four major peaks (624, 598, 556, and 502 cm^{-1}) in the higher frequencies region (> 500 cm^{-1}), and in the lower frequencies region (< 400 cm^{-1}) calculations showed red shifts of up to ~20 cm^{-1} as compared to the experiment. B3LYP corrects the blue shift at > 500 cm^{-1}, showing ~5 cm^{-1} deviation from the experiment at most in this area. While B3LYP better reproduces position of the peaks in the higher frequency region, PWPW91 has advantage of better reproducing the relative peak heights and NRVS spectra features over the wide range of frequencies (200–700 cm^{-1}). Overall, we found that discrepancies of ~5% between calculated and observed NRVS frequencies are the current stat-of-the-art and should not be used to rule out a particular hypothetical candidate structure.

Application of the NRVS technique to Hmd has provided the first information about the dynamics of the active site Fe-CO bending and stretching interactions. Because there is significant Fe motion in the Fe-CO bending and stretching modes, which range from 494 to 648 cm^{-1}, these modes give rise to the strongest features in the PVDOS spectrum. The NRVS data are thus strikingly different from patterns previously seen for mononuclear rubredoxin [46] or Fe-S clusters [28,44,47], where modes below 400 cm^{-1} dominate. Instead, the Hmd NRVS has some commonality with that of other organometallic complexes. For example, the strongest mode in the $[Fe(CN)_6]^{2-}$ PVDOS is a degenerate T_{1u} Fe-CN stretch at 600 cm^{-1} [20]. Even without simulations, the NRVS data for Hmd support a *cis*-$(CO)_2$ geometry for the active site, a conclusion already obtained from the mid-IR CO stretching modes [11]. A symmetric Fe-$(CO)_2$ stretch for a *trans*-$(CO)_2$ geometry would involve no Fe motion and hence would have no NRVS intensity.

In the region between ~200-400 cm^{-1}, the NRVS experiments provided information about the cysteine thiolate Fe-S bonding and the pyridone cofactor Fe-N ligation. We have assigned the peaks at ~274 cm^{-1} and ~311 cm^{-1} mostly to Fe-S stretching motion, while Fe-N(py) contributions are proposed to extend from the 274 cm^{-1} feature all the way down to 200 cm^{-1}.

The most problematic assignment involved the peak at 379 cm^{-1}. A 'tetrahedral' model for the Fe site lacked intensity in this region, yielding a significant mismatch with the NRVS, and allowing us to rule out this model. A simple way to mimic this feature was to include a water ligand and adjust the force constant to match. However, although not unheard of, water complexes with low spin Fe carbonyls are relatively rare [48]. We found that another way to obtain intensity in this region was to generate a 'truncated' model absent the fifth ligand. In this model, Fe-S(cys) stretching, coupled with other contributions, yields a reasonable simulation. The presence or absence of a water ligand remains an important unsolved question, which awaits better data with ^{18}O water samples.

NRVS was also used to probe for changes at the Fe site between pH 8 and pH 6 + methenyl-H_4MPT^+ + H_2 samples. Evidence for changes between these two conditions comes from differences in both infrared [11] and x-ray absorption spectra [12]. The modest NRVS spectral differences preclude major changes such as addition of a ligand or alteration of the Fe oxidation state. We thus consider what types of changes might be expected, based on the previous IR studies [11]. In the *v*CO region, under pH 8 or pH 6 under Ar, two strong IR bands were observed at 1944 and 2011 cm^{-1}. At pH 6, with the addition of methenyl-H_4MPT^+ and under H_2 atmosphere, the higher frequency band shifted and was interpreted as a ~50–50 mixture of 2011 and 2018 cm^{-1} peaks. An almost complete conversion to a band at 2017 cm^{-1} was seen with methenyl-H_4MPT and H_2. What might we expect in the *v*FeC region of the NRVS?

The correlation between *v*CO and *v*FeC frequencies has been studied extensively in heme proteins, where it has been used to distinguish between 'proximal' and 'distal' perturbations to the Fe site [41]. Distal effects are modifications around the CO pocket, and they can involve changes in hydrogen bonding to the CO or in the polarity of nearby ligands. For example, wild-type MbCO at pH 7.0 has a *v*CO at 1947 cm^{-1}, and the H64V mutant, in which the His64-CO H-bond is lost, has *v*CO at 1967 cm^{-1}. This distal effect also leads to a change in *v*FeC, from 507 cm^{-1} in wild type to 488 cm^{-1} in the mutant. Over a wide variety of 'distal' modifications, Spiro observed that on average, *v*FeC changes (in the opposite direction) by 75% of the change in *v*CO [41]. In contrast, a proximal change, such as replacement of the histidine trans to CO with a thiolate (as in cytochrome P-450), can yield the same *v*CO at 1947 cm^{-1} as wild-type MbCO, but with a shift to 473 cm^{-1} in *v*FeC.

If we presume that a similar correlation holds for *cis* $Fe(CO)_2$ complexes, then a ~6–7 cm^{-1} upshift in *v*CO with methenyl-H_4MPT^+ and H_2 *might* lead to a ~5–7 cm^{-1} downshift in *v*FeC. This is slightly less than the current monochromator resolution of 1 meV or ~ 8 cm^{-1}. However, if one looks closely at the 495 cm^{-1} *v*FeC region in the Hmd spectrum, for the methenyl-H_4MPT^+ and H_2 sample, there is an apparent broadening and shift in intensity to lower energy, compared to pH 8 conditions. Thus, the NRVS data are at least consistent with the IR results suggesting the production of a slightly different species under methenyl-H_4MPT^+ and H_2 conditions. The magnitude of the observed changes is consistent with a small perturbation such as a change in H-bonding, as opposed to a large change such as hydride binding directly to the Fe.

In summary, the NRVS results are consistent with previous FT-IR and EXAFS investigations, that have defined the minimal coordination sphere for Hmd Fe involving 4 ligands: two *cis*-CO groups, a cysteine thiolate, and a light atom that may be a nitrogen from the pyridone cofactor ring. The NRVS disfavors a strictly tetrahedral Fe site, but cannot yet distinguish between 5-coordinate models with a water ligand or 'truncated' 4-coordinate models. The modest changes under methenyl-H_4MPT^+ and H_2 conditions are interpreted as a change in hydrogen bonding and or conformation, as opposed to addition of an Fe ligand. The current results demonstrate that with the aid of DFT calculations, plus better signal-to-noise and resolution, as well as eventual crystallographic information about the Hmd active site

geometry, NRVS can play a role in elucidating the catalytic mechanism of this fascinating enzyme.

Supplementary Material

Refer to Web version on PubMed Central for supplementary material.

Acknowledgments

This work was funded by NIH GM-65440 (SPC), EB-001962 (SPC), GM-39914 (DAC), GM-061153 (TBR), and the DOE Office of Biological and Environmental Research (SPC). Seigo Shima and R. K. Thauer were supported by the Max Planck Society and by a grant from the Bundesministerium für Bildung und Forschung (BMBF) (BioH2 project). Use of the APS is supported by the DoE Office of Basic Energy Sciences. SPring-8 is funded by JASRI.

References

1. Zirngibl C, Hedderich R, Thauer RK. N^5, N^{10}-Methylenetetrahydromethanopterin dehydrogenase from *Methanobacterium thermoautotrophicum* has hydrogenase activity. FEBS Lett 1990;261:112–116.
2. Zirngibl C, van Dongen W, Schwörer B, von Bünau R, Richter M, Klein A, Thauer RK. H_2-forming methylenetetrahydromethanopterin dehydrogenase, a novel type of hydrogenase without iron-sulfur clusters in methanogenic archaea. Eur. J. Biochem 1992;208:511–520. [PubMed: 1521540]
3. Schleucher J, Griesinger C, Schwörer B, Thauer RK. H_2-Forming N^5,N^{10}-Methylenetetrahydromethanopterin Dehydrogenase from *Methanobacterium thermoautotrophicum* Catalyzes a Stereoselective Hydride Transfer As Determined by Two-Dimensional NMR Spectroscopy. Biochem 1994;33:3986–3983. [PubMed: 8142403]
4. Thauer RK, Klein AR, Hartmann GC. Reactions with Molecular Hydrogen in Microorganisms: Evidence for a Purely Organic Hydrogenation Catalyst. Chem. Rev 1996;97:3031–3042. [PubMed: 11848851]
5. Shima S, Thauer RK. A third type of hydrogenase catalyzing H_2 activation. Chem. Rec 2007;7:37–46. [PubMed: 17304591]
6. Klein AR, Thauer RK. Re-face specificity at C14a of methylenetetrahydromethanopterin and Si-face specificity at C5 of coenzyme F420 for coenzyme F420-dependent methylenetetrahydromethanopterin dehydrogenase from methanogenic Archaea. Eur. J. Biochem 1995;227:169–174. [PubMed: 7851382]
7. Buurman G, Shima S, Thauer RK. The metal-free hydrogenase from methanogenic archaea: evidence for a bound cofactor. FEBS Lett 2000;485:200–204. [PubMed: 11094167]
8. Lyon EJ, Shima S, Buurman G, Chowdhuri S, Batschauer A, Steinbach K, Thauer RK. UV-A/blue-light inactivation of the 'metal-free' hydrogenase (Hmd) from methanogenic archaea: the enzyme contains functional iron after all. Eur. J. Biochem 2004;271:195–204. [PubMed: 14686932]
9. Shima S, Lyon EJ, Sordel-Klippert M, Kauss M, Kahnt J, Thauer RK, Steinbach K, Xie X, Verdier L, Griesinger C. The cofactor of the iron-sulfur cluster free hydrogenase hmd: structure of the light-inactivation product. Angew. Chem. Int. Ed 2004;116:2547–2551.
10. Shima S, Lyon EJ, Thauer RK, Mienert B, Bill E. Mössbauer Studies of the Iron-Sulfur-Cluster-Free Hydrogenase: The Electronic State of the Mononuclear Fe Active Site. J. Am. Chem. Soc 2005;127:10430–10435. [PubMed: 16028957]
11. Lyon EJ, Shima S, Boecher R, Thauer RK, Grevels F-W, Bill E, Roseboom W, Albracht SPJ. Carbon Monoxide as an Intrinsic Ligand to Iron in the Active Site of the Iron-Sulfur-Cluster-Free Hydrogenase H_2-Forming Methylenetetrahydromethanopterin Dehydrogenase As Revealed by Infrared Spectroscopy. J. Am. Chem. Soc 2004;126:14239–14248. [PubMed: 15506791]
12. Korbas M, Vogt S, Meyer-Klaucke W, Bill E, Lyon EJ, Thauer RK, Shima S. The iron-sulfur-cluster-free hydrogenase (Hmd) is a metalloenzyme with a novel iron binding motif. 2006
13. Pilak O, Mamat Br, Vogt S, Hagemeier CH, Thauer RK, Shima S, Vonrhein C, Warkentin E, Ermler U. The Crystal Structure of the Apoenzyme of the Iron-Sulphur Cluster-free Hydrogenase. J. Mol. Biol 2006;358:798–809. [PubMed: 16540118]

14. Alp E, Sturhahn W, Toellner TS, Zhao J, Hu M, Brown DE. Vibrational Dynamics Studies by Nuclear Resonant Inelastic X-Ray Scattering. Hyp. Interact 2002;144/145:3–20.
15. Sturhahn W. Nuclear resonant spectroscopy. J. Phys. Cond. Matt 2004;16:S497–S530.
16. Leu BM, Zgierski MZ, Wyllie GRA, Scheidt WR, Sturhahn W, Alp EE, Durbin SM, Sage JT. Quantitative Vibrational Dynamics of Iron in Nitrosyl Porphyrins. J. Am. Chem. Soc 2004;126:4211–4227. [PubMed: 15053610]
17. Sturhahn W, Toellner TS, Alp EE, Zhang X, Ando M, Yoda Y, Kikuta S, Seto M, Kimball CW, Dabrowski B. Phonon Density of States Measured by Inelastic Nuclear Resonant Scattering. Phys. Rev. Lett 1995;74:3832–3835. [PubMed: 10058308]
18. Sage JT, Paxson C, Wyllie GRA, Sturhahn W, Durbin SM, Champion PM, Alp EE, Scheidt WR. Nuclear resonance vibrational spectroscopy of a protein active-site mimic. J. Phys.: Condens. Matter 2001;13:7707–7722.
19. Sturhahn W. CONUSS and PHOENIX: evaluation of nuclear resonant scattering data. Hyperfine Interact 2000;125:149–172.
20. Chumakov AI, Rüffer R, Leupold O, Sergueev I. Insight to Dynamics of Molecules with Nuclear Inelastic Scattering. Struct. Chem 2003;14:109–119.
21. Shima S, Thauer RK. Tetrahydromethanopterin-specific enzymes from *Methanopyrus kandleri*. Meth. Enzymol 2001;331:317–353. [PubMed: 11265475]
22. Venturi C, Bellachioma G, Cardaci G, Macchioni A, Zuccaccia C. Syntheses of di-hydrocarbyl derivatives of carbonyl phosphine complexes of iron. Inorg. Chim. Acta 2005;358:3815–3823.
23. Toellner T. Monochromatization of synchrotron radiation for nuclear resonant scattering experiments. Hyp. Int 2000;125:3–28.
24. Yoda Y, Yabashi M, Izumi K, Zhang XW, Kishimoto S, Kitao S, Seto M, Mitsui T, Harami T, Imai Y, Kikuta S. Nuclear resonant scattering beamline at SPring-8. Nucl. Inst. Meth. A 2001;467:715–718.
25. Kishimoto S, Yoda Y, Seto M, Kitao S, Kobayashi Y, Haruki R, Harami T. Array of avalanche photodiodes as a position-sensitive x-ray detector. Nucl. Inst. Meth. A 2004;513:193–196.
26. Shape Software. http://www.shapesoftware.com/
27. Dowty E. Fully automated microcomputer calculation of vibrational spectra. Phys. Chem. Minerals 1987;14:67–79.
28. Xiao Y, Fischer K, Smith MC, Newton W, Case DA, George SJ, Wang H, Sturhahn W, Alp EE, Zhao J, Yoda Y, Cramer SPJ. How Nitrogenase Shakes - Initial Information about P-Cluster and FeMo-Cofactor Normal Modes from Nuclear Resonance Vibrational Spectroscopy (NRVS). Am. Chem. Soc 2006;128:7608–7612.
29. Perdew JP, Chevary JA, Vosko SH, Jackson KA, Pederson MR, Singh DJ, Fiolhais C. Atoms, Molecules, Solids, and Surfaces - Applications of the Generalized Gradient Approximation for Exchange and Correlation. 1992;46:6671–6687.
30. Becke AD. Density-Functional Thermochemistry .3. the Role of Exact Exchange. 1993;98:5648–5652.
31. Jaguar, version 6.5. 2005.
32. Hay PJ, Wadt WR. Abinitio Effective Core Potentials for Molecular Calculations - Potentials for the Transition-Metal Atoms Sc to Hg. 1985;82:270–283.
33. Frisch MJ, Trucks GW, Schlegel HB, Scuseria GE, Robb MA, Cheeseman JR, Montgomery J, J JA, Vreven T, Kudin KN, Burant JC, Millam JM, Iyengar SS, Tomasi J, Barone V, Mennucci B, Cossi M, Scalmani G, Rega N, Petersson GA, Nakatsuji H, Hada M, Ehara M, Toyota K, Fukuda R, Hasegawa J, Ishida M, Nakajima T, Honda Y, Kitao O, Nakai H, Klene M, Li X, Knox JE, Hratchian HP, Cross JB, Bakken V, Adamo C, Jaramillo J, Gomperts R, Stratmann RE, Yazyev O, Austin AJ, Cammi R, Pomelli C, Ochterski JW, Ayala PY, Morokuma K, Voth GA, Salvador P, Dannenberg JJ, Zakrzewski VG, Dapprich S, Daniels AD, Strain MC, Farkas O, Malick DK, Rabuck AD, Raghavachari K, Foresman JB, Ortiz JV, Cui Q, Baboul AG, Clifford S, Cioslowski J, Stefanov BB, Liu G, Liashenko A, Piskorz P, Komaromi I, Martin RL, Fox DJ, Keith T, Al-Laham MA, Peng CY, Nanayakkara A, Challacombe M, Gill PMW, Johnson B, Chen W, Wong MW, Gonzalez C, Pople JA. GAUSSIAN 03. 2004

34. Cataliotti A, Foffani A, Marchetti L. Infrared Spectrum of Iron Pentacarbonyl. Inorg. Chem 1971;10:1594–1597.
35. Jones LH, McDowell RS, Goldblatt M, Swanson BI. Potential Constants of Iron Pentacarbonyl from Vibrational Spectra of Isotopic Species. J. Chem. Phys 1972;57:2050–2064.
36. Yu N-T, Benko B, Kerr EA, Gersonde K. Iron-carbon bond lengths in carbonmonoxy and cyanomet complexes of the monomeric hemoglobin III from *Chironomus thummi*: A critical comparison between resonance Raman and x-ray diffraction studies. Proc. Nat. Acad. Sci 1984;81:5106–5110. [PubMed: 6591180]
37. Hu S, Vogel KM, Spiro TG. Deformability of Heme Protein CO Adducts: FT-IR Assignment of the FeCO Bending Mode. J. Am. Chem. Soc 1994;116:11187–11188.
38. Ghosh A, Bocian DF. Carbonyl Tilting and Bending Potential Energy Surface of Carbon Monoxyhemes. J. Phys. Chem 1996;100:6363–6367.
39. Nakamoto, K. Infrared and Raman Spectra of Inorganic and Coordination Compounds. Vol. 5th ed.. New York: Wiley-Interscience; 1997.
40. Stec B, Phillips GN Jr. How the CO in myoglobin acquired its bend: lessons in interpretation of crystallographic data. Acta. Crys 2001;D57:751–754.
41. Spiro TG, Wasbotten IHJ. CO as a vibrational probe of heme protein active sites. Inorg. Biochem 2005;99:34–44.
42. Jegat C, Fouassier M, Mascetti J. Carbon Dioxide Coordination Chemistry. 1. Vibrational Study of *trans*-$Mo(CO_2)_2(PMe_3)_2$ and $Fe(CO_2)(PMe_3)_4$. Inorg. Chem 1991;30:1521–1529.
43. Scheidt WR, Durbin SM, Sage JT. Nuclear resonance vibrational spectroscopy -- NRVS. J. Inorg. Biochem 2005;99:60–71. [PubMed: 15598492]
44. Xiao Y, Koutmos M, Case DA, Coucouvanis D, Wang H, Cramer SP. Dynamics of an $[Fe_4S_4(SPh)_4]^{2-}$ Cluster Explored *via* IR, Raman, and Nuclear Resonance Vibrational Spectroscopy (NRVS) - Analysis using ^{36}S Substitution, DFT Calculations, and Empirical Force Fields. Dalton Trans 2006:2192–2201. [PubMed: 16673033]
45. Tan M-L, Bizzarri AR, Xiao Y, Cannistraro S, Ichiye T, Manzoni C, Cerullo G, Adams MWW, Francis E, Jenney J, Cramer SP. Observation of Terahertz Vibrations in *Pyrococcus furiosus* Rubredoxin *via* Impulsive Coherent Vibrational Spectroscopy and Nuclear Resonance Vibrational Spectroscopy – Interpretation by Molecular Mechanics. J. Inorg. Biochem 2006;101:375–384. [PubMed: 17204331]
46. Xiao Y, Wang H, George SJ, Smith MC, Adams MWW, Francis E, Jenney J, Sturhahn W, Alp EE, Zhao J, Yoda Y, Dey A, Solomon EI, Cramer SP. Normal Mode Analysis of *Pyrococcus furiosus* Rubredoxin via Nuclear Resonant Vibrational Spectroscopy (NRVS) and Resonance Raman Spectroscopy. J. Am. Chem. Soc 2005;127:14596–14606. [PubMed: 16231912]
47. Xiao Y, Tan M, Ichiye T, Wang H, Smith MC, Meyer J, Sturhahn W, Alp EE, Zhao J, Yoda Y, Cramer SP. Dynamics of *Rhodobacter capsulatus* [2Fe-2S] Ferredoxin VI and *Aquifex aeolicus* Ferredoxin 5 *via* Nuclear Resonance Vibrational Spectroscopy (NRVS) and Resonance Raman Spectroscopy. Biochem 2007;46submitted
48. Jeffery JC, Odell B, Stevens N, Talbot RE. Self assembly of a novel water soluble iron(II) macrocyclic phosphine complex from tetrakis(hydroxymethyl)phosphonium sulfate and iron(II) ammonium sulfate: single crystal X-ray structure of the complex $[Fe(H_2O)_2\{RP(CH_2N(CH_2PR_2)CH_2)_2PR\}]SO_4\cdot 4H_2O$(R = CH_2OH). Chem. Commun 2000:101–102.

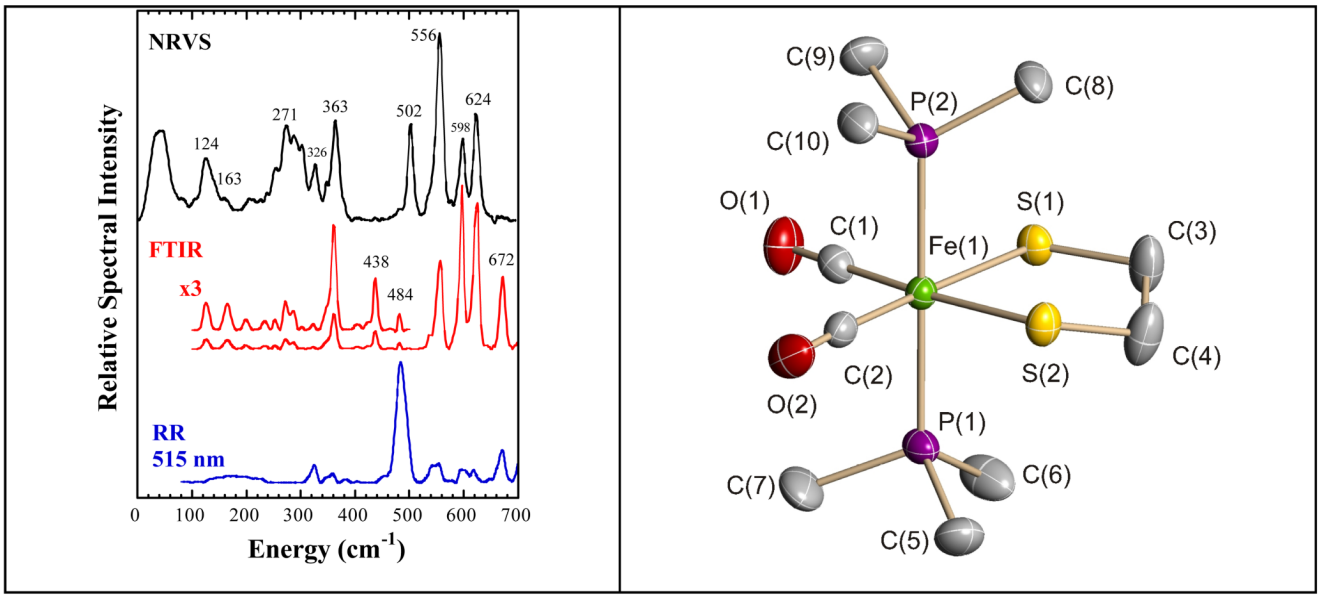

Figure 1.

(Left) NRVS PVDOS (—), far infrared (—), and resonance Raman (—) for $Fe(S_2C_2H_4)(CO)_2(PMe_3)_2$. Right: Molecular structure of $Fe(S_2C_2H_4)(CO)_2(PMe_3)_2$. Thermal ellipsoids are set at the 50% probability level. Hydrogen atoms are omitted for clarity. Key distances (Å) and angles (°): Fe(1)–C(1) 1.766(3), Fe(1)–C(2) 1.773(3), Fe(1)–P(2) 2.2628(9), Fe(1)–P(1) 2.2780(9), Fe(1)–S(2) 2.3181(11), Fe(1)-S(1) 2.3355(9); C(1)–Fe(1)–C(2) 97.56(13), C(1)–Fe(1)–P(2) 91.03(9), C(2)–Fe(1)–P(2) 92.22(9), C(1)–Fe(1)–P(1) 89.37(9), C(2)–Fe(1)–P(1) 87.27(9), P(2)–Fe(1)–P(1) 179.38(3), C(1)–Fe(1)–S(2) 174.70(10), C(2)–Fe(1)–S(2) 87.68 (11), P(2)–Fe(1)–S(2) 87.92(3), P(1)–Fe(1)–S(2) 91.73(3), C(1)–Fe(1)–S(1) 86.22(9), C(2)–Fe(1)–S(1) 176.18(11), P(2)–Fe(1)–S(1) 87.17(4), P(1)–Fe(1)–S(1) 93.32(3), S(2)–Fe(1)–S(1) 88.53(3).

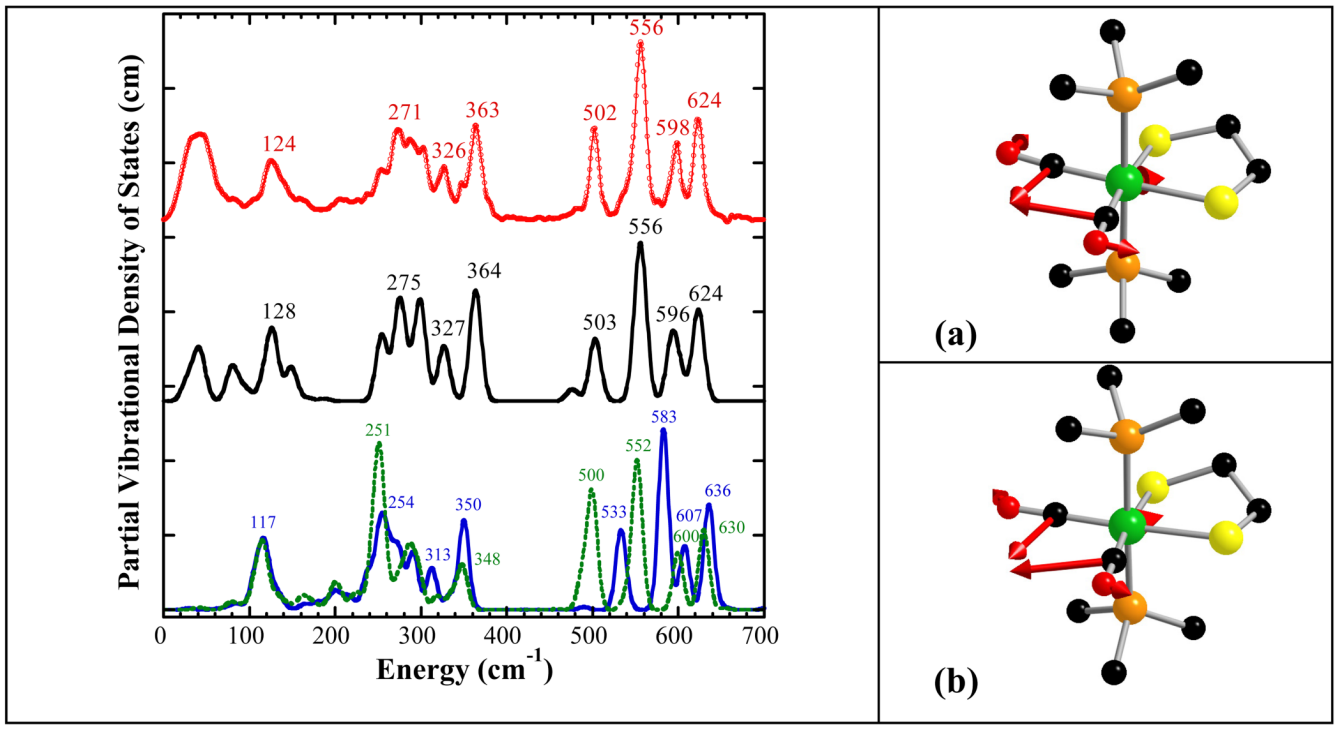

Figure 2.

Left: (top to bottom) NRVS PVDOS (∘ ∘ ∘), Vibratz simulation (—), and DFT simulations using LACV3P**+ basis and PWPW91 functional (—) or B3LYP functional (– –) for Fe $(S_2C_2H_4)(CO)_2(PMe_3)_2$. Right: atomic motion in normal modes at (a) 626 cm^{-1} in Vibratz simulation, (b) 636 cm^{-1} in DFT simulation using PWPW91 functional and LACV3P**+ basis.

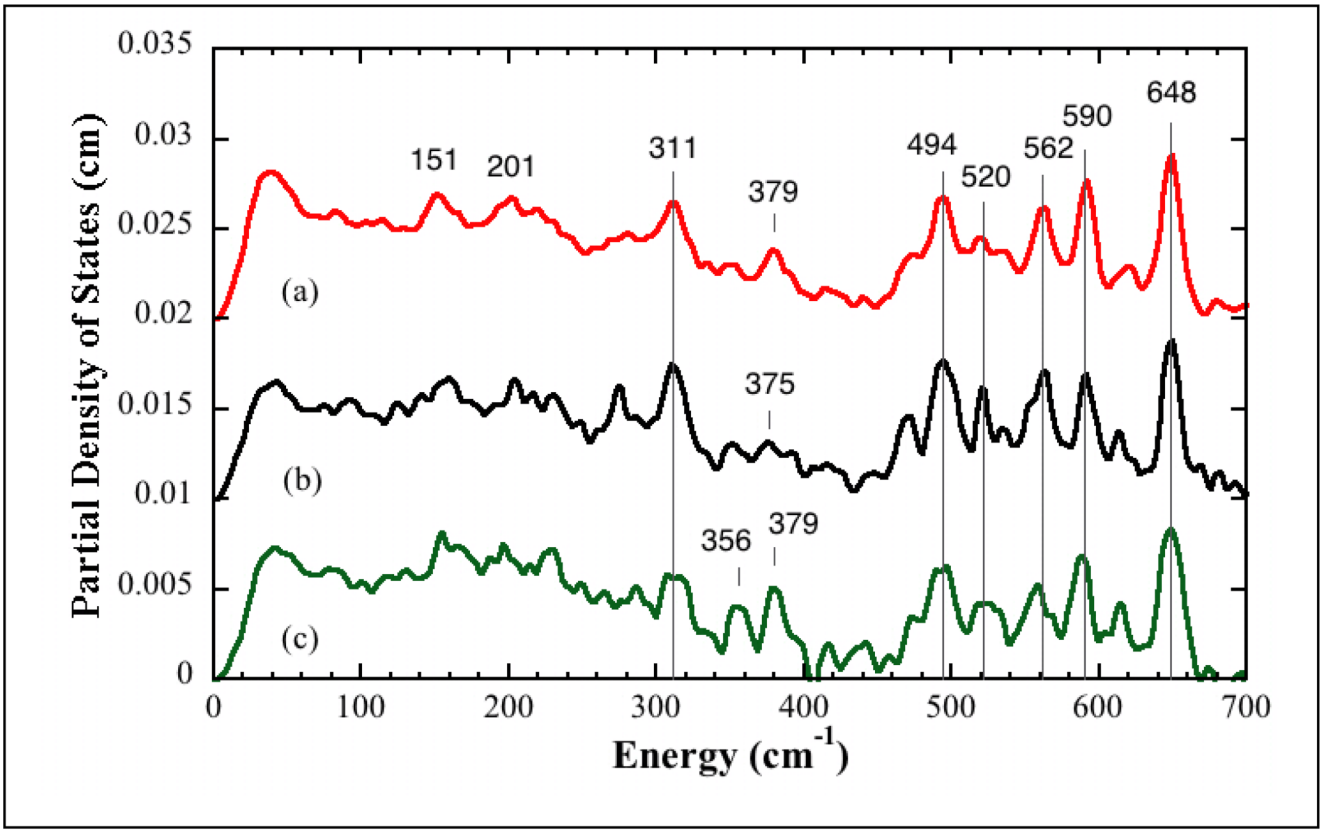

Figure 3.
NRVS PVDOS for (top-to-bottom): (a) Hmd in 50 mM Tricine/NaOH buffer at pH 8.0, (b) Hmd 50 mM Tricine/NaOH buffer exchanged in ^{18}O water at pH 8.0, (c) Hmd + methenyl-H_4MPT^+ + H_2 in 50 mM Mes-NaOH buffer at pH 6.0.

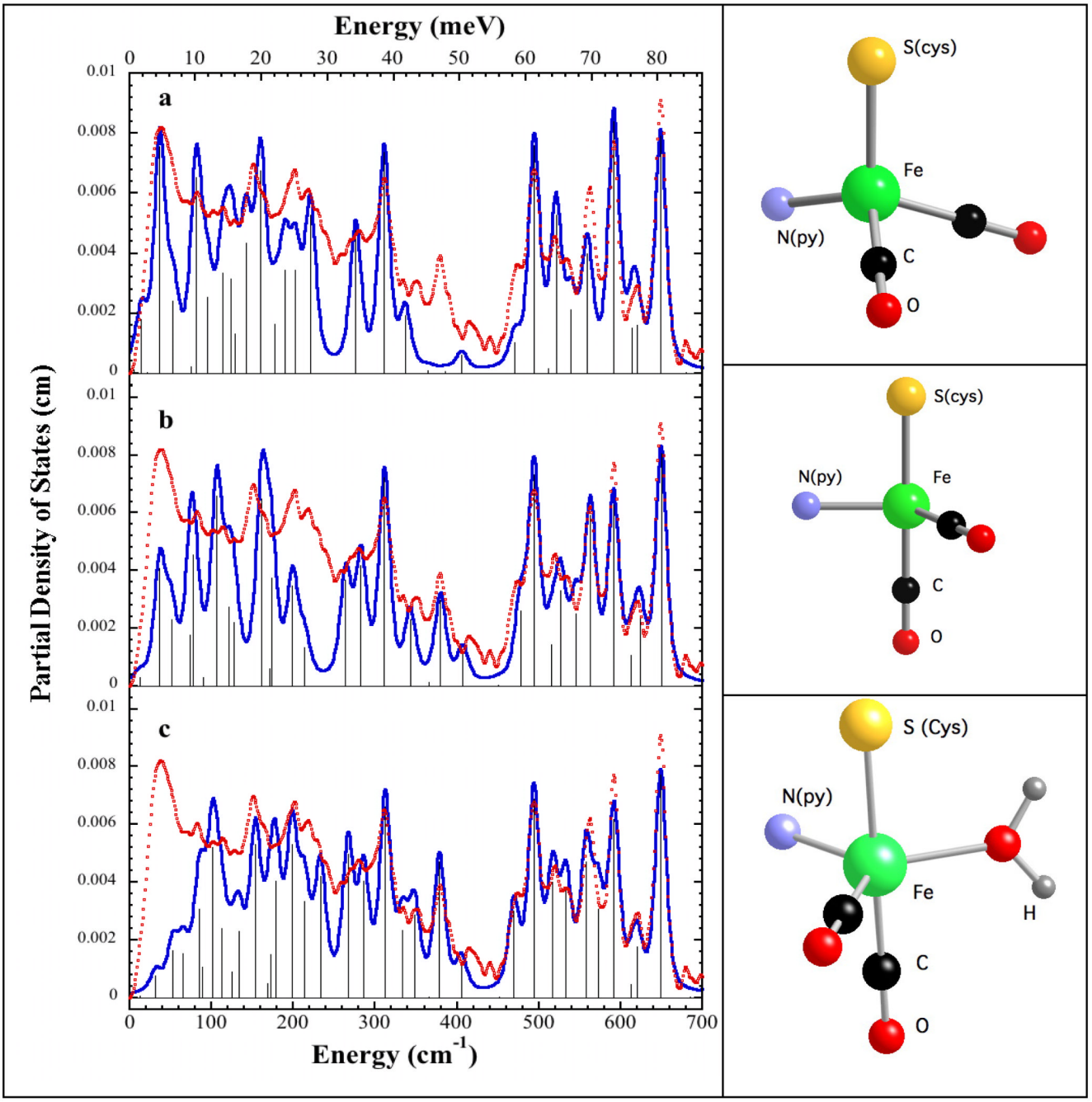

Figure 4.

Left: Fe partial vibrational density of state functions for Hmd at pH 8 (∘ ∘ ∘) in natural abundance water and simulations (—) for (top to bottom): 'tetrahedral' model, 4-coordinate 'truncated' model, 5-coordinate 'trigonal bipyramidal' model with ^{16}O water ligand. Right: Ball and stick models of the structures employed in the calculations. Additional cysteine and pyridone atoms have been omitted for clarity.

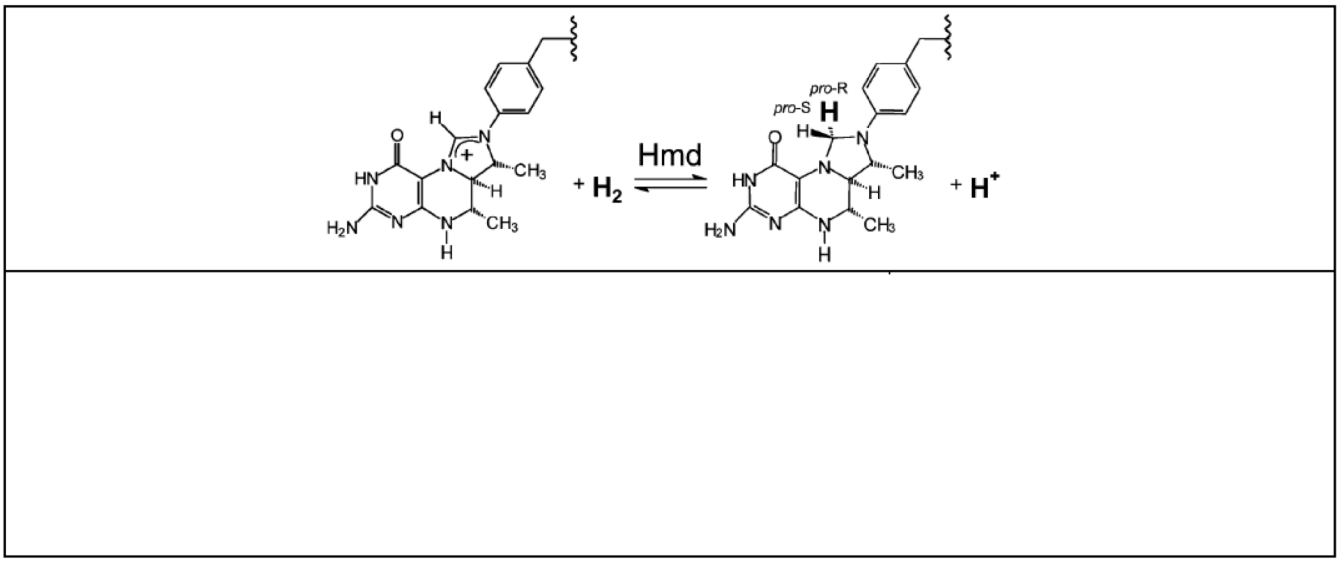

Chart 1.
Top: the reaction catalyzed by Hmd. Bottom: Hmd cofactor breakdown product formed after UV-A irradiation [9].